research article

Image reconstruction using small-voxel size improves small lesion detection for positron emission tomography

Sebastijan Rep[1,2], Petra Tomse[1,3], Luka Jensterle[1], Leon Jarabek[4], Katja Zaletel[1,5], Luka Lezaic[1,5]

[1] Department for Nuclear Medicine, University Medical Centre Ljubljana, Slovenia
[2] Faculty of Health Sciences, University of Ljubljana, Slovenia
[3] Faculty of Mathematics and Physics, University of Ljubljana, Slovenia
[4] Department of Radiology, General Hospital Novo Mesto, Slovenia
[5] Faculty of Medicine, University of Ljubljana, Slovenia

Radiol Oncol 2022; 56(2): 142-149.

Received 1 February 2022
Accepted 16 February 2022

Correspondence to: Luka Ležaić, M.D., Ph.D., Department for Nuclear Medicine, University Medical Centre Ljubljana, Zaloška 7, 1525 Ljubljana, Slovenia. E-mail: luka.lezaic@kclj.si

Disclosure: No potential conflicts of interest were disclosed.

Background. PET/CT imaging is widely used in oncology and provides both metabolic and anatomic information. Because of the relatively poor spatial resolution of PET, the detection of small lesions is limited. The low spatial resolution introduces the partial-volume effect (PVE) which negatively affects images both qualitatively and quantitatively. The aim of the study was to investigate the effect of small-voxel (2 mm in-line pixel size) *vs.* standard-voxel (4 mm in-line pixel size) reconstruction on lesion detection and image quality in a range of activity ratios.

Materials and methods. The National Electrical Manufacturers Association (NEMA) body phantom and the Micro Hollow-Sphere phantom spheres were filled with a solution of [^{18}F]fluorodeoxyglucose ([^{18}F]FDG) in sphere-to-background ratios of 2:1, 3:1, 4:1 and 8:1. In all images reconstructed with 2 mm and 4 mm in-line pixel size the visual lesion delineation, contrast recovery coefficient (CRC) and contrast-to-noise ratio (CNR) were evaluated.

Results. For smaller (≤ 13 mm) phantom spheres, significantly higher CRC and CNR using small-voxel reconstructions were found, also improving visual lesion delineation. CRC did not differ significantly for larger (≥ 17 mm) spheres using 2 mm and 4 mm in-line pixel size, but CNR was significantly lower; however, lower CNR did not affect visual lesion delineation.

Conclusions. Small-voxel reconstruction consistently improves precise small lesion delineation, lesion contrast and image quality.

Key words: PET/CT; voxel size; contrast recovery coefficient; contrast-to-noise ratio

Introduction

Positron emission tomography combined with computed tomography (PET/CT) is widely used for staging and tumour response assessment in oncology.[1-3] PET/CT provides both metabolic and anatomic information and allows detection, localization and characterization of the lesions.[4-5] In the majority of PET/CT scanners image reconstruction is traditionally performed using the 4 mm in-line pixel size (4 x 4 x 4 mm voxel).[6-8] This relatively large voxel size affects image quality by limiting the image spatial resolution, which limits the detection of small metabolically active lesions.[9-11] The poor spatial resolution additionally introduces the partial-volume effect (PVE), negatively affecting images both visually and quantitatively, resulting in the decrease of signal in smaller lesions and im-

age smoothing. The PVE can be reduced by using a smaller in-line pixel size and consequently voxel size during image reconstruction. Smaller voxel sizes have already been studied in the preclinical as well as clinical setting, demonstrating both qualitative and quantitative improvement in reconstructed images.[12-14] However, the majority of previous preclinical studies evaluated the image quality of small-voxel reconstruction using phantoms with high target/background ratio.[13] The goal of our study was to explore the effect of small-voxel reconstruction on the image quality systematically in a set of low-to-high target-to-background ratios reflecting realistic clinical scenarios in focused imaging for small lesions.

Materials and methods

Phantom preparation

Acquisitions and reconstructions were performed with the National Electrical Manufacturers Association (NEMA) International Electrotechnical Commission (IEC) body phantom and the Micro Hollow-Sphere phantom. The NEMA body phantom consists of the background compartment with a volume of 9700 ml and six fillable spheres with diameters of 10, 13, 17, 22, 28 and 37 mm. The background compartment was in all instances filled with the specific activity of [^{18}F] fluorodeoxyglucose ([^{18}F] FDG) solution of 5.3 kBq/mL ± 5%. Filling of the spheres was performed with 42 kBq/mL (ratio 8:1), 21.2 kBq/mL (ratio 4:1), 16.1 kBq/mL (ratio 3:1) and 10.4 kBq/mL (ratio 2:1). The Micro Hollow-Sphere phantom with background compartment volume 120 mL and four fillable spheres with diameters of 4, 5, 6 and 8 mm was filled with identical specific activities.

Acquisition and reconstruction

Phantoms were scanned for each activity ratio on a Siemens Biograph mCT Flow Edge (True V) PET/CT scanner combining patented lutetium oxyorthosilicate (LSO) PET system with time-of-flight (TOF) technique and a 128-slice CT. The PET component of this system consists of four rings of 48 detector blocs with each bloc containing 169 detector elements (detector element dimension of 4 x 4 x 20 mm), PET axial field-of-view (FOV) of 221 mm, coincidence window of 4.1 nsec, system energy resolution ≤ 12 % full width at half maximum (FWHM) and typical system time resolution of 540 psec. The acquisition protocol included a low dose (120 kV; 25 mA) non-enhanced CT scan for the attenuation correction, followed by a 10 min single bed position 3D PET acquisition.

All PET scans were reconstructed using a Siemens True-X-TOF iterative algorithm (2 iterations, 21 subsets) which incorporates point-spread-function (PSF) and TOF correction (SIEMENS ultra HD PET©). Each image was reconstructed using 4 mm and 2 mm in-plane pixel dimensions and zoom factor of 1; 200 x 200 and 400 x 400 matrix size was used for 4 and 2 mm in-plane pixel size reconstruction.

Image analysis

Quantitative image analysis was performed on SYNGO VIA processing software. For each activity ratio, spherical volumes of interest (VOIs) were manually placed over the hot spheres of the NEMA body and the Micro Hollow-Sphere phantom images, using the known sphere diameter limits. In addition, six spherical background VOIs (diameter of 20 mm) were centred in the same transaxial plane as the hot spheres in the NEMA body phantom and one spherical background VOI (diameter of 40 mm) in a homogeneous region of the background of the Micro Hollow Sphere phantom. Mean and maximum [^{18}F]FDG activity concentrations (CAm_{mean}) and CAm_{max}) in kilobequerel/mililiter (kBq/ml) were determined for each VOI with SYNGO VIA. All lesions were assessed qualitatively for localization and delineation.

Mean and maximum contrast recovery coefficient (CRC) and contrast-to-noise ratio (CNR) were calculated to quantitatively compare the detectability of lesions between different voxel size reconstructions.

Mean and maximum CRC for each phantom sphere was calculated as the ratio between mean/maximum measured activity concentration (CAm_{mean} and CAm_{max}) and true activity concentration (CAt):

$$CRC_{mean} = CAm_{mean}/CAt; \quad CRC_{max} = CAm_{max}/CAt \qquad \text{Eq. [A.1]}$$

Mean and maximum CNR was calculated as a measure of the signal level in the presence of noise:

$$CNR_{mean} = (CAm_{mean}\text{-}CAbg)/SDbg; \quad CNR_{max} = (CAm_{max}\text{-}CAbg)/SDbg \qquad \text{Eq. [A.2]}$$

where CAbg is the average measured activity concentration in the background and SDbg is the

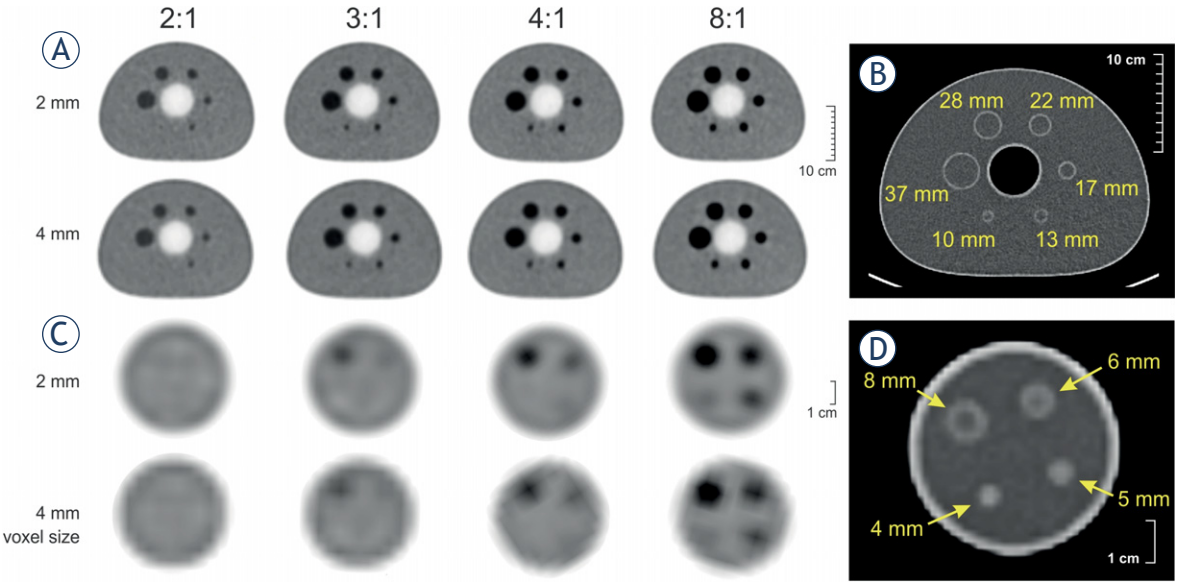

FIGURE 1. NEMA body **(A)** and the Micro Hollow-Sphere phantom **(C)**, filled in the sphere-to-background radioactivity ratio 2:1, 3:1, 4:1, 8:1, and reconstructed with 2 mm (top row) and 4 mm (bottom row) in-line pixel size. Axial CT images with phantom spheres diameter of NEMA body **(B)** and the Micro Hollow-Sphere phantom **(D)**.

standard deviation of the activity concentration in the background.

CRC and CNR were analyzed independently in three ways: for spheres with diameters ≤ 13 mm (smaller spheres), for spheres with diameters ≥ 17 mm (larger spheres), and for all spheres combined, respectively (13). Only lesions that were visible at both 2 mm and 4 mm in-line pixel sizes reconstructions were analysed.

Statistical analysis

The normality of the distribution of CRC_{mean}, CRC_{max}, CNR_{mean}, CNR_{max} values was assessed us-

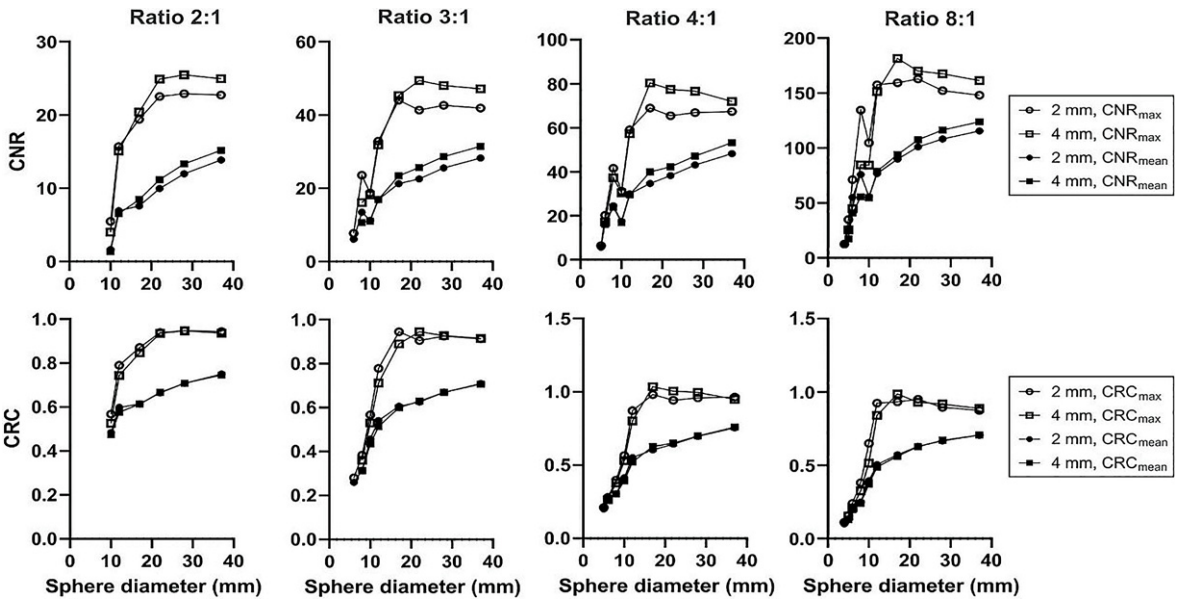

FIGURE 2. Measurements of contrast-to-noise ratio $(CNR)_{max/mean}$ (top row) and contrast recovery coefficient $(CRC)_{max/mean}$ (bottom row) in all NEMA body and the Micro Hollow-Sphere phantom spheres for all radioactivity concentration ratios with 2 mm and 4 mm in-line pixel size.

TABLE 1. Contrast recovery coefficient $(CRC)_{max}$, CRC_{mean}, of the four Micro Hollow Sphere phantom and the six NEMA body phantom spheres filled with sphere-to-background radioactivity concentration ratios of 2:1, 3:1, 4:1, 8:1 for both 2 mm and 4 mm in-line pixel size reconstructions, including relative changes in %

	Micro Hollow Sphere phantom - sphere diameter (mm)					NEMA body phantom - sphere diameter (mm)				
Ratio 8:1	4 mm	5 mm	6 mm	8 mm	10 mm	13 mm	17 mm	22 mm	28 mm	37 mm
2 mm max	0.11	0.16	0.24	0.38	0.65	0.92	0.93	0.95	0.89	0.87
4 mm max	N/A	0.15	0.21	0.33	0.51	0.84	0.99	0.93	0.92	0.89
% change		2	14	17	26	10	-5	2	-2	-2
2 mm mean	0.10	0.14	0.20	0.25	0.39	0.50	0.57	0.63	0.67	0.71
4 mm mean	N/A	0.13	0.19	0.24	0.37	0.49	0.56	0.63	0.67	0.71
% change		4	2	3	6	3	2	0	0	0
Ratio 4:1	4 mm	5 mm	6 mm	8 mm	10 mm	13 mm	17 mm	22 mm	28 mm	37 mm
2 mm max	N/A	0.21	0.28	0.40	0.57	0.87	0.98	0.94	0.96	0.96
4 mm max	N/A	N/A	0.26	0.38	0.53	0.80	1.03	1.00	1.00	0.95
% change			6	5	8	9	-5	-6	-4	2
2 mm mean	N/A	0.20	0.26	0.30	0.41	0.55	0.60	0.64	0.70	0.75
4 mm mean	N/A	N/A	0.26	0.30	0.39	0.52	0.63	0.64	0.70	0.75
% change			0	0	5	6	-4	-1	0	-1
Ratio 3:1	4 mm	5 mm	6 mm	8 mm	10 mm	13 mm	17 mm	22 mm	28 mm	37 mm
2 mm max	N/A	N/A	0.28	0.38	0.57	0.78	0.94	0.90	0.92	0.91
4 mm max	N/A	N/A	N/A	0.36	0.53	0.71	0.89	0.94	0.93	0.91
% change				7	7	9	6	-1	0	0
2 mm mean	N/A	N/A	0.26	0.31	0.64	0.54	0.61	0.62	0.67	0.71
4 mm mean	N/A	N/A	N/A	0.31	0.43	0.51	0.60	0.63	0.67	0.71
% change				1	5	5	1	-1	0	0
Ratio 2:1	4 mm	5 mm	6 mm	8 mm	10 mm	13 mm	17 mm	22 mm	28 mm	37 mm
2 mm max	N/A	N/A	N/A	N/A	0.57	0.79	0.87	0.94	0.95	0.94
4 mm max	N/A	N/A	N/A	N/A	0.53	0.74	0.85	0.93	0.95	0.93
% change					8	6	3	0	0	1
2 mm mean	N/A	N/A	N/A	N/A	0.48	0.60	0.61	0.66	0.71	0.75
4 mm mean	N/A	N/A	N/A	N/A	0.47	0.58	0.61	0.67	0.71	0.74
% change					2	4	0	-1	0	1

N/A = not applicable

ing the Shapiro-Wilk test. Median, minimum and maximum for these parameters were calculated. We assessed the differences between 2 mm and 4 mm in-line pixel sizes using the Wilcoxon signed-rank test for paired samples.

Statistical analysis was performed using IBM SPSS Statistics for Windows, version 25 (IBM Corp., Armonk, N.Y., USA) with p-values < 0.05 considered as statistically significant. GraphPad Prism version 8.0.0 for Windows (GraphPad Software, San Diego, California USA, www.graphpad.com) was used to create the artwork.

The study does not include patient data and therefore does not require the approval of the ethics committee.

Results

NEMA body and the Micro Hollow-Sphere phantom images reconstructed with 2 mm and 4 mm in-line pixel sizes for all concentration ratios are presented in Figure 1.

TABLE 2. Contrast-to-noise ratio $(CNR)_{max}$, CNR_{mean}, of the four Micro Hollow Sphere phantom and the six NEMA body phantom spheres filled with sphere-to-background radioactivity concentration ratios of 2:1, 3:1, 4:1, 8:1 for both 2 mm and 4 mm voxel size reconstructions, including relative changes in %

	Micro Hollow Sphere phantom - sphere diameter (mm)					NEMA body phantom - sphere diameter (mm)				
Ratio 8:1	4 mm	5 mm	6 mm	8 mm	10 mm	13 mm	17 mm	22 mm	28 mm	37 mm
2 mm max	12.53	34.82	71.23	134.50	104.68	157.51	159.30	162.70	152.06	148.02
4 mm max	N/A	25.58	44.71	84.76	84.32	151.31	181.45	169.86	167.41	161.28
% change		36	59	59	24	4	-12	-4	-9	-8
2 mm mean	11.99	24.84	55.10	75.80	55.69	76.75	89.86	100.92	108.16	115.50
4 mm mean	N/A	17.41	40.95	55.58	54.73	78.83	93.99	107.44	116.37	123.83
% change		43	35	36	2	-3	-4	-6	-7	-7
Ratio 4:1	4 mm	5 mm	6 mm	8 mm	10 mm	13 mm	17 mm	22 mm	28 mm	37 mm
2 mm max	N/A	6.33	20.19	41.57	31.20	59.06	68.97	65.49	66.91	67.42
4 mm max	N/A	N/A	17.13	37.28	30.46	57.33	80.41	77.47	76.63	71.95
% change			18	12	2	3	-14	-15	-13	-6
2 mm mean	N/A	5.73	16.51	24.55	17.42	29.96	34.68	38.24	43.13	48.28
4 mm mean	N/A	N/A	16.04	23.93	16.91	29.57	39.95	42.28	47.14	53.26
% change			3	3	3	1	-13	-10	-9	-9
Ratio 3:1	4 mm	5 mm	6 mm	8 mm	10 mm	13 mm	17 mm	22 mm	28 mm	37 mm
2 mm max	N/A	N/A	7.72	23.53	18.69	32.87	44.04	41.32	42.66	41.87
4 mm max	N/A	N/A	N/A	16.13	18.18	31.84	45.27	49.36	48.04	47.15
% change				46	3	3	-10	-8	-9	-9
2 mm mean	N/A	N/A	6.11	13.45	11.28	16.93	21.28	22.58	25.55	28.23
4 mm mean	N/A	N/A	N/A	10.66	11.01	16.91	23.39	25.56	28.58	31.47
% change				26	2	0	9	-9	-9	-9
Ratio 2:1	4 mm	5 mm	6 mm	8 mm	10 mm	13 mm	17 mm	22 mm	28 mm	37 mm
2 mm max	N/A	N/A	N/A	N/A	5.49	15.68	19.40	22.51	22.90	22.73
4 mm max	N/A	N/A	N/A	N/A	4.00	15.08	20.40	24.89	25.48	24.94
% change					37	4	-5	-10	-10	-9
2 mm mean	N/A	N/A	N/A	N/A	1.64	6.93	7.59	9.95	11.97	13.85
4 mm mean	N/A	N/A	N/A	N/A	1.37	6.54	8.44	11.18	13.32	15.18
% change					20	6	-10	-11	-10	-9

N/A = not applicable

Visual comparison of the images demonstrates enhanced contrast and delineation of smaller (≤ 13 mm) spheres in images reconstructed with 2 mm compared to 4 mm in-line pixel size. In the sphere-to-background activity ratio of 2:1, the sphere with 10 mm diameter in NEMA body phantom was still visible in the 2 mm in-line pixel size reconstruction, but not in 4 mm in-line pixel size reconstruction. In the sphere-to-background activity ratio 2:1, the spheres in Micro Hollow-Sphere phantom were not visible in both reconstructions. However, in higher sphere-to-background activity ratios, the contrast and delineation of spheres in Micro Hollow-Sphere phantom were clearly superior in the 2 mm in-line pixel size reconstruction; furthermore, in the activity ratio of 4:1, the 5 mm sphere was still visible in the 2 mm in-line pixel size reconstruction, but not in 4 mm in-line pixel size reconstruction. For larger (≥ 17 mm) spheres the delineation was also superior with 2 mm in-line pixel size reconstruction, perhaps with the exception of the highest (8:1) sphere-to-background activity ratio.

For quantitative assessment, measurements of CRC and CNR in all phantom spheres of NEMA

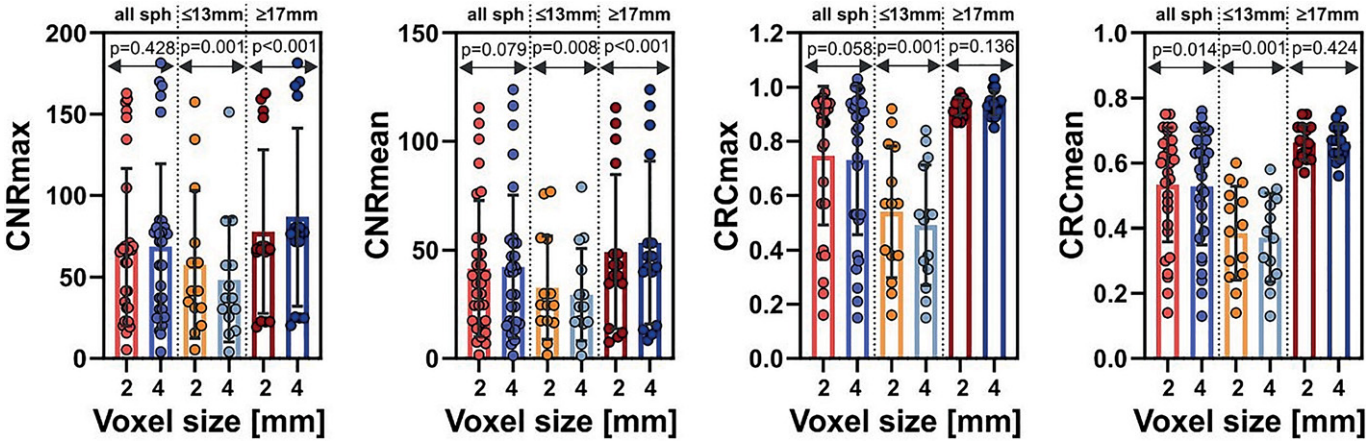

FIGURE 3. Graphically represented contrast recovery coefficient $(CRC)_{max/mean}$ and contrast-to-noise ratio $(CNR)_{max/mean}$ of the 2 mm and 4 mm in-line pixel sizes.

body phantom and Micro Hollow-Sphere phantom for all activity ratios are presented in Tables 1 and 2 and graphically in Figure 2. Median, minimum and maximum values for both parameters are presented in Tables 3 and 4.

From the combined measurements in both phantoms we found that in the smaller (≤ 13 mm) spheres the CRC values were significantly higher in the images reconstructed using the 2 mm in comparison to the 4 mm in-line pixel size (CRC_{max}: p = 0.001, CRC_{mean}: p = 0.001). On the other hand, CRC did not differ significantly between the 2 mm and 4 mm in-line pixel sizes for larger (≥ 17 mm) spheres (CRC_{max}: p = 0.136, CRC_{mean}: p = 0.424). For all spheres combined CRC_{max} values also did not differ significantly between the two voxel sizes for large spheres (p = 0.058), but were significantly higher for CRC_{mean} (p = 0.014).

CNR was found to be significantly higher for reconstruction with 2 mm compared to 4 mm in-line pixel size for smaller (≤ 13 mm) spheres (CNR_{max}, p = 0.001 and CNR_{mean}, p = 0.008). In addition, CNR was elevated in 2 mm reconstructed images when analyzing all spheres in all sphere-to-background radioactivity ratio (CNR_{max}: p = 0.428, CNR_{mean}: p = 0.079). However, in larger (≥ 17 mm) spheres CNR was significantly lower in 2 mm in-line pixel size images compared to the 4 mm (CNR_{max}: p = < 0.001, CNR_{mean}: p = < 0.001); nevertheless, as stated above, the visual delineation of larger lesions was not hampered by lower CNR.

The comparison of $CRC_{max/mean}$ and $CNR_{max/mean}$ between the two in-line pixel sizes is graphically presented in Figure 3.

Discussion

The aim of the present study was to evaluate the potential advantages of small-voxel reconstruction on PET image quality. While confirming the results of previous preclinical work of similar design[13] using high target-to-background ratios, we also found the advantages of small-voxel reconstruction to translate as well towards lower ratios, resembling realistic clinical circumstances when focused imaging is performed for limited body sections in extended duration, such as parathyroid or brain PET.[15,16] However, these findings may translate to acquisitions typically used for whole-body imaging as well, as recently shown in a preclinical study.[17]

The 4 mm in-line pixel size reconstruction is routinely used in most PET centres worldwide in clinical practice, resulting in relatively poor spatial resolution and consequently limited visualization and quantification of small lesions. Using the NEMA body and Micro Hollow-Sphere phantom with various target-to-background activity concentration ratios we were able to demonstrate that the delineation and quantification of small lesions can be improved if reconstruction with 2 mm in-line pixel size is used. While the use of even smaller (1 mm) in-line pixel size may seem advantageous for the purpose of small lesion detection, the lesion contrast appears to plateau at 2 mm in-line pixel size in comparison to the standard 4 mm in-line pixel size reconstruction.[18]

Qualitatively, the use of 2 mm in-line pixel reconstruction improves the spatial resolution with

TABLE 3. Median, minimum and maximum values of contrast recovery coefficient $(CRC)_{max}$ and CRC_{mean} over all for all spheres, spheres ≤ 13 mm and spheres ≥ 17 mm. The values are given for images reconstructed with 2 mm and 4 mm voxel size

	Number of spheres	Median	Minimum	Maximum
CRC_{max} 2 mm	30	0.88	0.16	0.98
CRC_{max} 4 mm	30	0.87	0.13	1.03
CRC_{mean} 2 mm	30	0.60	0.14	0.75
CRC_{mean} 4 mm	30	0.59	0.13	0.76
CRC_{max} 2 mm; ≤ 13 mm	14	0.56	0.16	0.92
CRC_{max} 4 mm; ≤ 13 mm	14	0.52	0.13	0.84
CRC_{mean} 2 mm; ≤ 13 mm	14	0.40	0.14	0.60
CRC_{mean} 4 mm; ≤ 13 mm	14	0.38	0.13	0.60
CRC_{max} 2 mm; ≥ 17 mm	16	0.94	0.87	0.98
CRC_{max} 4 mm; ≥ 17 mm	16	0.94	0.87	1.03
CRC_{mean} 2 mm; ≥ 17 mm	16	0.66	0.57	0.75
CRC_{mean} 4 mm; ≥ 17 mm	16	0.66	0.56	0.76

TABLE 4. Median, minimum and maximum values of contrast-to-noise ratio $(CNR)_{max}$ and CNR_{mean} over all spheres-to-background ratios for all spheres, smaller (≤ 13 mm) spheres and larger (≥ 17 mm) spheres. The values are given for images reconstructed with 2 mm and 4 mm in-line pixel size

	Number of spheres	Median	Minimum	Maximum
CNR_{max} 2 mm	30	42.26	5.49	162.60
CNR_{max}4 mm	30	46.21	4.00	181.45
CNR_{mean} 2 mm	30	25.56	1.64	115.50
CNR_{mean} 4 mm	30	27.15	1.37	123.83
CNR_{max} 2 mm; ≤ 13 mm	14	33.84	5.49	157.51
CNR_{max} 4 mm; ≤ 13 mm	14	31.15	4.00	151.31
CNR_{mean} 2 mm; ≤ 13 mm	14	20.98	1.64	76.75
CNR_{mean} 4 mm; ≤ 13 mm	14	17.16	1.37	78.73
CNR_{max} 2 mm; ≥ 17 mm	16	54.76	19.40	162.70
CNR_{max} 4 mm; ≥ 17 mm	16	60.65	20.40	181.45
CNR_{mean} 2 mm; ≥ 17 mm	16	31.45	7.59	115.50
CNR_{mean} 4 mm; ≥ 17 mm	16	35.71	8.44	123.83

improved visualization of the smaller (≤ 13 mm) spheres in comparison to the standard approach. The qualitative impression was confirmed with quantitative analysis: across the evaluated activity ratios, improved mean and maximum CRC and CNR were demonstrated for smaller (≤ 13 mm) lesions, suggesting higher lesion detectability. Increase in CRC directly affects standard uptake value (SUV) as the predominant quantitative imaging metric.[19] With the use of small voxels, the image noise inevitably statistically increases. However, as again demonstrated for smaller (≤ 13 mm) lesions, the increased noise is compensated through improved CNR. These findings confirm and extend the existing results in the preclinical setting[6,13]; the likely explanation is the reduction of PVE through the use of small voxels, leading to reduction in averaging and increased activity in smaller lesions.[20] Several approaches are increasingly being used to reduce the effect of noise on image quality and improve spatial resolution, such as time-of-flight (TOF) and point-spread function (PSF) corrections[5,7,8,19,21-24], typically integrated into routine vendor-specific PET reconstruction protocols. Small-voxel reconstruction was shown to provide additional improvement in small lesion detection when both approaches are already used[19]; nevertheless, the possibility of introducing artefacts and potential false-positive findings related to PSF modelling and small-voxel reconstruction must be considered.[9]

The existing literature evaluating the effect of small-voxel reconstruction in the clinical setting is similarly limited and is focused on small lesions. Extending the work from the preclinical setting[13], one group was able to demonstrate that the detection and quantitative assessment (standardized uptake values for lesions and target-to-background ratios) significantly improves for metastatic lymph nodes in patients with breast cancer when small-voxel reconstruction with 2 mm in-line pixel size is used.[14] In a similar report in patients with head and neck squamous cell carcinoma, the detection and quantitative assessment of metastatic lymph nodes as well as image quality was improved with larger image matrix size (2 mm in-line pixel size).[12] Currently, the existing literature demonstrating improved performance of small-voxel reconstruction in the clinical setting is limited on the evaluation of lymph nodes in staging of malignant disease – a typical indication for clinical PET imaging. Nevertheless, in other conditions in which PET imaging is increasingly being used for evaluation of small lesions (such as preoperative localization of hyperfunctioning parathyroid tissue[25], similar benefit can be expected. While an important limitation of the present work and other preclinical studies lies in the design with homogenous background activity and known location of the evaluated lesions, the listed clinical examples demonstrate the potential of small-voxel reconstruction for routine clinical application.

Conclusions

The use of small-voxel reconstruction in PET imaging provides consistent improvement in small lesion localization and delineation, lesion contrast and image quality.

Authors' contributions

SR: performed the all imaging and analysis of NEMA phantom, and was a major contributor in writing; PT: contributor in writing, review and editing; LJ: writing-analysis of NEMA phantom, review and editing; KZ: writing-review and editing; LL: writing-review and editing

References

1. Derlin T, Grünwald V, Steinbach J, Wester HJ, Ross TL. Molecular imaging in oncology using positron emission tomography. *Dtsch Arztebl Int* 2018; **115:** 175-81. doi: 10.3238/arztebl.2018.0175
2. Simianu VV, Varghese TK, Flanagan MR, Flum DR, Shankaran V, Oelschlager BK, et al. Positron emission tomography for initial staging of esophageal cancer among medicare beneficiaries. *J Gastrointest Oncol* 2016; **7:** 395-402. doi: 10.21037/jgo.2015.10.03
3. Juweid ME, Stroobants S, Hoekstra OS, Mottaghy FM, Dietlein M, Guermazi A, et al. Use of positron emission tomography for response assessment of lymphoma: consensus of the Imaging Subcommittee of International Harmonization Project in Lymphoma. *J Clin Oncol* 2007; **25:** 571-8. doi: 10.1200/JCO.2006.08.2305
4. Schöder H, Erdi YE, Larson SM, Yeung HWD. PET/CT: a new imaging technology in nuclear medicine. *Eur J Nucl Med Mol Imaging* 2003; **30:** 1419-37. doi: 10.1007/s00259-003-1299-6
5. Townsend DW. Dual-modality imaging: combining anatomy and function. *J Nucl Med* 2008; **49:** 938-55. doi: 10.2967/jnumed.108.051276
6. Kolthammer JA, Su KH, Grover A, Narayanan M, Jordan DW, Muzic RF. Performance evaluation of the Ingenuity TF PET/CT scanner with a focus on high count-rate conditions. *Phys Med Biol* 2014; **59:** 3843-59. doi: 10.1088/0031-9155/59/14/3843
7. Conti M. Focus on time-of-flight PET: the benefits of improved time resolution. *Eur J Nucl Med Mol Imaging* 2011; **38:** 1147-57. doi: 10.1007/s00259-010-1711-y
8. Boellaard R, Delgado-Bolton R, Oyen WJG, Giammarile F, Tatsch K, Eschner W, et al. FDG PET/CT: EANM procedure guidelines for tumour imaging: version 2.0. *Eur J Nucl Med Mol Imaging* 2015; **42:** 328-54. doi: 10.1007/s00259-014-2961-x
9. van der Vos CS, Koopman D, Rijnsdorp S, Arends AJ, Boellaard R, van Dalen JA, et al. Quantification, improvement, and harmonization of small lesion detection with state-of-the-art PET. *Eur J Nucl Med Mol Imaging* 2017; **44(Suppl 1):** 4-16. doi: 10.1007/s00259-017-3727-z
10. Fukui MB, Blodgett TM, Meltzer CC. PET/CT imaging in recurrent head and neck cancer. *Semin Ultrasound CT MR* 2003; **24:** 157-63. doi: 10.1016/s0887-2171(03)90037-0
11. Tarantola G, Zito F, Gerundini P. PET instrumentation and reconstruction algorithms in whole-body applications. *J Nucl Med* Off Publ Soc Nucl Med 2003; **44:** 756-69. PMID: 12732678
12. Li CY, Klohr S, Sadick H, Weiss C, Hoermann K, Schoenberg SO, et al. Effect of time-of-flight technique on the diagnostic performance of 18F-FDG PET/CT for assessment of lymph node metastases in head and neck squamous cell carcinoma. *J Nucl Med Technol* 2014; **42:** 181-7. doi: 10.2967/jnmt.114.141192
13. Koopman D, van Dalen JA, Lagerweij MCM, Arkies H, de Boer J, Oostdijk AHJ, et al. Improving the detection of small lesions using a state-of-the-art time-of-flight PET/CT system and small-voxel reconstructions. *J Nucl Med Technol* 2015; **43:** 21-7. doi: 10.2967/jnmt.114.147215
14. Koopman D, van Dalen JA, Arkies H, Oostdijk AHJ, Francken AB, Bart J, et al. Diagnostic implications of a small-voxel reconstruction for loco-regional lymph node characterization in breast cancer patients using FDG-PET/CT. *EJNMMI Res* 2018; **8:** 3. doi: 10.1186/s13550-018-0359-7
15. Petranović Ovčariček P, Giovanella L, Carrió Gasset I, Hindié E, Huellner MW, Luster M, et al. The EANM practice guidelines for parathyroid imaging. *Eur J Nucl Med Mol Imaging* 2021; **48:** 2801-22. doi: 10.1007/s00259-021-05334-y
16. Guedj E, Varrone A, Boellaard R, Albert NL, Barthel H, van Berckel B, et al. EANM procedure guidelines for brain PET imaging using [18F]FDG, version 3. *Eur J Nucl Med Mol Imaging* 2022; **49:** 632-51. doi: 10.1007/s00259-021-05603-w
17. Øen SK, Aasheim LB, Eikenes L, Karlberg AM. Image quality and detectability in Siemens Biograph PET/MRI and PET/CT systems-a phantom study. *EJNMMI Phys* 2019; **6:** 16. 10.1186/s40658-019-0251-1
18. Adler S, Seidel J, Choyke P, Knopp MV, Binzel K, Zhang J, et al. Minimum lesion detectability as a measure of PET system performance. *EJNMMI Phys* 2017; **4:** 13. doi: 10.1186/s40658-017-0179-2
19. Jakoby BW, Bercier Y, Conti M, Casey ME, Bendriem B, Townsend DW. Physical and clinical performance of the mCT time-of-flight PET/CT scanner. *Phys Med Biol* 2011; **56:** 2375-89. doi: 10.1088/0031-9155/56/8/004
20. Meechai T, Tepmongkol S, Pluempitiwiriyawej C. Partial-volume effect correction in positron emission tomography brain scan image using super-resolution image reconstruction. *Br J Radiol* 2015; **88(1046):** 20140119. doi: 10.1259/bjr.20140119
21. Lee YS, Kim JS, Kim KM, Kang JH, Lim SM, Kim H-J. Performance measurement of PSF modeling reconstruction (True X) on Siemens Biograph TruePoint TrueV PET/CT. *Ann Nucl Med* 2014; **28:** 340-8. doi: 10.1007/s12149-014-0815-z
22. Lois C, Jakoby BW, Long MJ, Hubner KF, Barker DW, Casey ME, et al. An assessment of the impact of incorporating time-of-flight information into clinical PET/CT imaging. *J Nucl Med* 2010; **51:** 237-45. doi: 10.2967/jnumed.109.068098
23. Rogasch JM, Steffen IG, Hofheinz F, Großer OS, Furth C, Mohnike K, et al. The association of tumor-to-background ratios and SUVmax deviations related to point spread function and time-of-flight F18-FDG-PET/CT reconstruction in colorectal liver metastases. *EJNMMI Res* 2015; **5:** 31. doi: 10.1186/s13550-015-0111-5.
24. Akamatsu G, Ishikawa K, Mitsumoto K, Taniguchi T, Ohya N, Baba S, et al. Improvement in PET/CT image quality with a combination of point-spread function and time-of-flight in relation to reconstruction parameters. *J Nucl Med* 2012; **53:** 1716-22. doi: 10.2967/jnumed.112.103861
25. Treglia G, Piccardo A, Imperiale A, Strobel K, Kaufmann PA, Prior JO, et al. Diagnostic performance of choline PET for detection of hyperfunctioning parathyroid glands in hyperparathyroidism: a systematic review and meta-analysis. *Eur J Nucl Med Mol Imaging* 2019; **46:** 751-65.